

Cosmographic parameters from current and next-generation gravitational wave detectors

Jonathan Morais,^a Rodrigo Gonçalves,^{b,a} Jailson Alcaniz^a

^aObservatório Nacional, Rio de Janeiro - RJ, 20921-400, Brasil

^bDepartamento de Física, Universidade Federal Rural do Rio de Janeiro, Seropédica - RJ, 23897-000, Brasil

E-mail: jmorais@on.br; rsg_goncalves@ufrj.br; alcaniz@on.br

Abstract. We evaluate the capability of current and next-generation gravitational wave detectors, such as Advanced LIGO, Einstein Telescope and DECIGO, to constrain cosmographic parameters using electromagnetically bright standard sirens. By adopting a third-order Taylor expansion, we analyze how signal-to-noise ratios and the number of events impact the estimates of the Hubble constant (H_0), the deceleration (q_0) and jerk (j_0) parameters. Our results show that while Advanced LIGO provides a calibration-free measurement of H_0 at the few-percent level, it remains insensitive to higher-order parameters. In contrast, the Einstein Telescope and DECIGO reach sub-percent accuracy for H_0 . Notably, DECIGO achieves a precision better than 10% for the deceleration parameter q_0 and a few tens of percent for the jerk parameter j_0 .

Contents

1	Introduction	1
2	Cosmography	2
3	Methodology	5
3.1	Gravitational Waves Source Distribution	7
3.2	Gravitational Waves Detection	9
3.3	Parameter Estimation	11
4	Results	13
4.1	SNR Analysis	13
4.2	N Analysis	16
5	Conclusions	18
A	Numerical Results for the SNR-based and N Analysis	23

1 Introduction

The advent of multi-messenger gravitational wave (GW) astronomy has provided a novel research field to investigate both astrophysical processes and fundamental aspects of gravity and cosmology [1]. The first GW signal [2] was detected on September 14, 2015, by the two detectors of the Laser Interferometer gravitational wave Observatory (LIGO) [3]. Since then, the second-generation detectors, including LIGO, Virgo [4], and KAGRA [5], have confirmed more than 200 events [6], establishing GWs as a powerful new tool to investigate the Universe. In the next decade is expected the beginning of operations from the third-generation detectors such as the Einstein Telescope (ET) [7] and the Deci-hertz Interferometer gravitational wave Observatory (DECIGO) [8]. With their improved sensitivity, detections of coalescing binaries are expected to become as common as other probes, allowing us to study the Universe with much higher precision.

From a cosmological perspective, however, even under optimistic assumptions, the current GW observations still have a limited impact. Among the hundreds of confirmed events nowadays, only one has a direct redshift measurement [9]. This measurement is crucial, since gravitational waves from compact binary coalescences can act as *standard sirens* [10]: the GW analogs of standardizable candles [11] in electromagnetic astronomy. This terminology arises because the characteristic *chirp* waveform allows a direct measurement of the luminosity distance (d_L), independent of the cosmic distance ladder. However, the source redshift (z) cannot be uniquely determined from the GW signal alone due to a degeneracy between the intrinsic masses of the binary components and the redshift, which manifests as a degeneracy with d_L and can be broken only with additional information.

One such possibility arises when an electromagnetic counterpart is observed, enabling the identification of the host galaxy and, consequently, a direct measurement of the redshift. Several events involving at least one neutron star were followed up in search of such counterparts, including GW190425 [12], as well as the neutron star–black hole mergers GW200105 and GW200115 [13]; however, no confirmed association was found. This was successfully achieved for the binary neutron star merger GW170817, which was observed together with the short gamma-ray burst GRB170817A [14]. Events of this kind, for which both the luminosity distance and the redshift are measured, are known as *bright sirens* [15]. They provide a powerful and direct way to constrain cosmological parameters and to test the expansion history of the Universe [16]. The next generation of interferometers is expected to detect a much larger number of bright sirens due to their enhanced sensitivities [17], which will allow more precise and systematic studies of cosmology using gravitational wave observations [18–20].

Conversely, GW detections without an observed electromagnetic counterpart define the class of *dark sirens* [21]. In these cases, the redshift information must be inferred statistically, for instance through cross-correlation with galaxy catalogs [22], probabilistic host-galaxy association or hierarchical Bayesian inference frameworks that combine population models with large-scale structure information [23]. While dark sirens represent a promising way to extract cosmological information from the growing GW catalog, this work focuses on bright sirens, for which the redshift can be measured with negligible uncertainty. This enables a model-independent reconstruction of the luminosity distance–redshift relation $d_L(z)$, without assuming a specific cosmological background, within the framework of the so-called *cosmographic approach* [24].

In this paper, we forecast the constraining power of current and next-generation gravitational-wave detectors, such as Advanced LIGO, the Einstein Telescope, and DECIGO, using electromagnetically bright standard sirens. Adopting a third-order Taylor expansion, we examine how the signal-to-noise ratio and the number of observed events influence the reconstruction of the Hubble constant H_0 , as well as the deceleration q_0 and jerk parameters j_0 . The paper is organized as follows: Sec. 2 provides a concise overview of the cosmographic expansion. The simulated catalogs and the methodology adopted for the statistical analysis are described in Sec. 3. The main results are presented and discussed in Sec. 4. Finally, Sec. 5 summarizes the main conclusions drawn from our analysis.

2 Cosmography

We begin by assuming a homogeneous, isotropic, and spatially flat Universe, described by the Friedmann–Lemaître–Robertson–Walker (FLRW) metric (with $c = 1$):

$$ds^2 = -dt^2 + a^2(t) [dr^2 + r^2(d\theta^2 + \sin^2 \theta d\phi^2)], \quad (2.1)$$

where t denotes cosmic time and $a(t)$ is the scale factor. In order to study the expansion history in a model-independent way, we follow [25] and expand the scale factor as a

Taylor series around the present cosmic time t_0 :

$$\begin{aligned} \frac{a(t)}{a(t_0)} = 1 + H_0(t - t_0) - \frac{1}{2}q_0[H_0(t - t_0)]^2 + \frac{1}{6}j_0[H_0(t - t_0)]^3 \\ + \frac{1}{24}s_0[H_0(t - t_0)]^4 + \frac{1}{120}l_0[H_0(t - t_0)]^5 + \frac{1}{720}m_0[H_0(t - t_0)]^6 + \mathcal{O}(7), \end{aligned} \quad (2.2)$$

where H_0 is the Hubble constant at the present epoch, and the higher-order derivatives of the scale factor define the following cosmographic parameters:

$$\begin{aligned} q_0 &= -\frac{1}{H_0^2} \left(\frac{1}{a} \frac{d^2 a}{dt^2} \right) \Big|_{t=t_0}, & j_0 &= \frac{1}{H_0^3} \left(\frac{1}{a} \frac{d^3 a}{dt^3} \right) \Big|_{t=t_0}, & s_0 &= \frac{1}{H_0^4} \left(\frac{1}{a} \frac{d^4 a}{dt^4} \right) \Big|_{t=t_0}, \\ l_0 &= \frac{1}{H_0^5} \left(\frac{1}{a} \frac{d^5 a}{dt^5} \right) \Big|_{t=t_0}, & m_0 &= \frac{1}{H_0^6} \left(\frac{1}{a} \frac{d^6 a}{dt^6} \right) \Big|_{t=t_0}. \end{aligned} \quad (2.3)$$

The parameters q_0 , j_0 , s_0 , l_0 and m_0 are respectively referred to as the *deceleration*, *jerk*, *snap*, *lerk* and *crackle* parameters. These quantities provide a purely kinematical description of the cosmic expansion and are defined by successive time derivatives of the scale factor evaluated at the present cosmic time.

By applying the definition of redshift, $1 + z \equiv a(t_0)/a(t)$ to Eq. (2.2), with $a(t_0) = 1$, one can express the Hubble parameter as a function of redshift [26], given by:

$$\begin{aligned} H(z) = H_0 &\left[1 + (1 + q_0)z + \frac{1}{2}(j_0 - q_0^2)z^2 + \frac{1}{6}(3q_0^2 + 3q_0^3 - 4q_0j_0 - 3j_0 - s_0)z^3 \right. \\ &+ \frac{1}{24}(-12q_0^2 - 24q_0^3 - 15q_0^4 + 32q_0j_0 + 25q_0^2j_0 + 7q_0s_0 + 12j_0 - 4j_0^2 + 8s_0 + l_0)z^4 \\ &+ \frac{1}{120}(m_0 - 60q_0^2 - 180q_0^3 - 225q_0^4 - 105q_0^5 - 10j_0^2(6 + 7q_0) + l_0(15 + 11q_0) \\ &\left. + 15j_0(4 + 16q_0 + 25q_0^2 + 14q_0^3 - s_0) + 60s_0 + 105q_0s_0 + 60q_0^2s_0\right)z^5 + \mathcal{O}(z^6) \Big]. \end{aligned} \quad (2.4)$$

We can use Eq. (2.4) to define other distance functions relevant in cosmology. In particular, for our analysis it is convenient to express the *luminosity distance* in terms

of the cosmographic expansion

$$\begin{aligned}
d_L(z) = & \frac{1}{H_0} \left[z + \frac{1}{2}(1 - q_0)z^2 + \left(-\frac{1}{6} - \frac{j_0}{6} + \frac{q_0}{6} + \frac{q_0^2}{2} \right) z^3 \right. \\
& + \left(\frac{1}{12} + \frac{5j_0}{24} - \frac{q_0}{12} + \frac{5j_0q_0}{12} - \frac{5q_0^2}{8} - \frac{5q_0^3}{8} + \frac{s_0}{24} \right) z^4 \\
& + \left(-\frac{1}{20} - \frac{9j_0}{40} + \frac{j_0^2}{12} - \frac{l_0}{120} + \frac{q_0}{20} - \frac{11j_0q_0}{12} + \frac{27q_0^2}{40} - \frac{7j_0q_0^2}{8} \right. \\
& \quad \left. + \frac{11q_0^3}{8} + \frac{7q_0^4}{8} - \frac{11s_0}{120} - \frac{q_0s_0}{8} \right) z^5 \\
& + \left(\frac{1}{30} + \frac{7j_0}{30} - \frac{19j_0^2}{72} + \frac{19l_0}{720} + \frac{m_0}{720} - \frac{q_0}{30} + \frac{13j_0q_0}{9} - \frac{7j_0^2q_0}{18} \right. \\
& \quad \left. + \frac{7l_0q_0}{240} - \frac{7q_0^2}{10} + \frac{133j_0q_0^2}{48} - \frac{13q_0^3}{6} + \frac{7j_0q_0^3}{4} - \frac{133q_0^4}{48} \right. \\
& \quad \left. - \frac{21q_0^5}{16} + \frac{13s_0}{90} - \frac{7j_0s_0}{144} + \frac{19q_0s_0}{48} + \frac{7q_0^2s_0}{24} \right) z^6 + \mathcal{O}(z^7) \Big]. \quad (2.5)
\end{aligned}$$

The Taylor expansion employed in cosmography suffers from convergence issues at high redshifts. As discussed by [25], the series expansion of cosmological quantities in terms of the redshift z has a finite radius of convergence, set by the nearest singularity in the complex z -plane. In particular, the transformation $1+z = a(t_0)/a(t)$ implies the presence of a pole at $z = -1$, corresponding to the limit $a \rightarrow \infty$. As a consequence, the Taylor series about $z = 0$ converges only within $|z| < 1$. Therefore, although the series is formally defined for positive redshifts, it becomes unreliable for $z \gtrsim 1$, where the expansion lies outside its radius of convergence and truncation errors grow rapidly. This limitation directly affects the luminosity distance $d_L(z)$, whose Taylor series can diverge or lose precision for sources at intermediate or high redshifts, thus compromising its reliability in those regimes. To achieve better convergence at larger redshifts, alternative parameterizations have been proposed, such as the y -redshift [27, 28], or rational approximations like the Padé [29], Chebyshev [30] expansions, among others [31].

However, exploring these alternative formulations lies beyond the scope of the present work, where we restrict our analysis to the standard expansion in terms of the usual z -redshift. Thus to circumvent the convergence limitations, we restrict our analysis to data with redshifts $z < 1$, where the Taylor expansion remains a valid approximation. Within this regime, we systematically explore the highest expansion order that provides the best agreement with the fiducial luminosity distance predicted by the adopted cosmological model, minimizing the relative deviation between the cosmographic and theoretical curves. This analysis will be further detailed in the following section.

3 Metodology

In order to investigate how the luminosity distance expansion at different orders deviates from a given cosmological model, we first define the fiducial cosmology that will serve as the reference framework for our simulations. This model corresponds to the standard Λ CDM cosmology, characterized by the matter density parameter $\Omega_m = 0.311$ and the Hubble constant $H_0 = 67.66 \text{ km s}^{-1} \text{ Mpc}^{-1}$, in agreement with the most recent Cosmic Microwave Background (CMB) measurements [32]. It is worth noting that the same theoretical analysis was also performed using the SH0ES estimations for both parameters [33], yielding to practically identical results. Therefore, the particular choice of H_0 does not significantly affect our conclusions.

To determine the values of the cosmographic parameters, we adopt the analytical expressions derived within the Λ CDM framework [34]. Explicitly, the cosmographic parameters in Eq. (2.3) can be expressed in terms of one another (see Eq. (4) in [34]). By substituting the standard Λ CDM Hubble function $H(z) = H_0 \sqrt{\Omega_m(1+z)^3 + 1 - \Omega_m}$, we obtain the corresponding relations

$$\begin{aligned} q_0 &= \frac{3}{2}\Omega_m - 1, \\ j_0 &= 1, \\ s_0 &= 1 - \frac{9}{2}\Omega_m, \\ l_0 &= 1 + 3\Omega_m - \frac{27}{2}\Omega_m^2, \\ m_0 &= 1 - \frac{27}{2}\Omega_m^2 - 81\Omega_m^2 - \frac{81}{2}\Omega_m^3. \end{aligned} \tag{3.1}$$

Using the abovementioned matter density parameter in combination with Eq. (3.1), the numerical values of the corresponding cosmographic parameters are summarized in Table 1.

q_0	j_0	s_0	l_0	m_0
-0.533	1	-0.4	0.627	-9.365

Table 1: Cosmographic parameters in a flat Λ CDM cosmology with $\Omega_m = 0.311$.

We can now calculate the luminosity distance using Eq. (2.5) and the fiducial parameters listed in Table 1, considering the redshift range $z < 1$ due to the convergence issues discussed previously. In Fig. 1, we present the behavior of d_L as a function of redshift for different truncation orders of the cosmographic series. For comparison, the fiducial Λ CDM model is also shown (black dashed curve). The bottom panel displays the relative difference between each cosmographic approximation and the fiducial model.

This comparison allows to determine the most suitable truncation order for our analysis. As can be seen, the series truncated at third order deviates by less than 1%

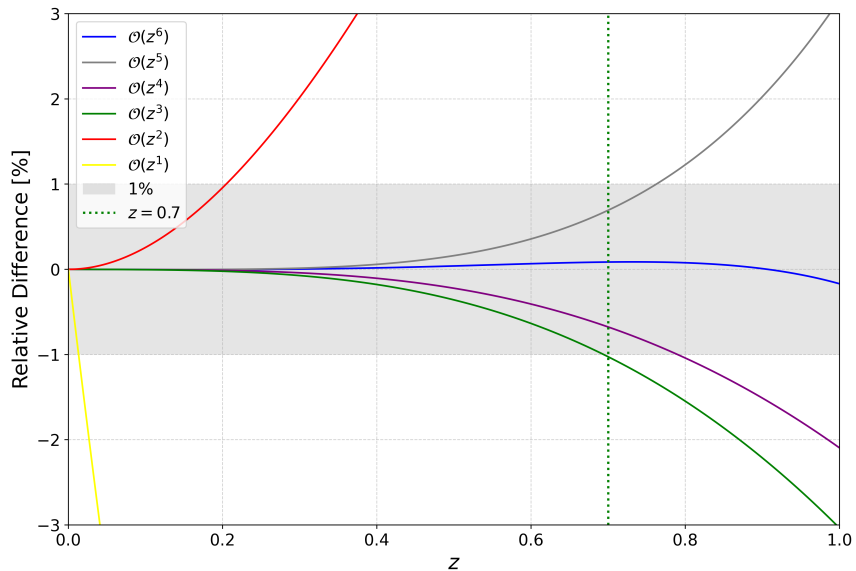
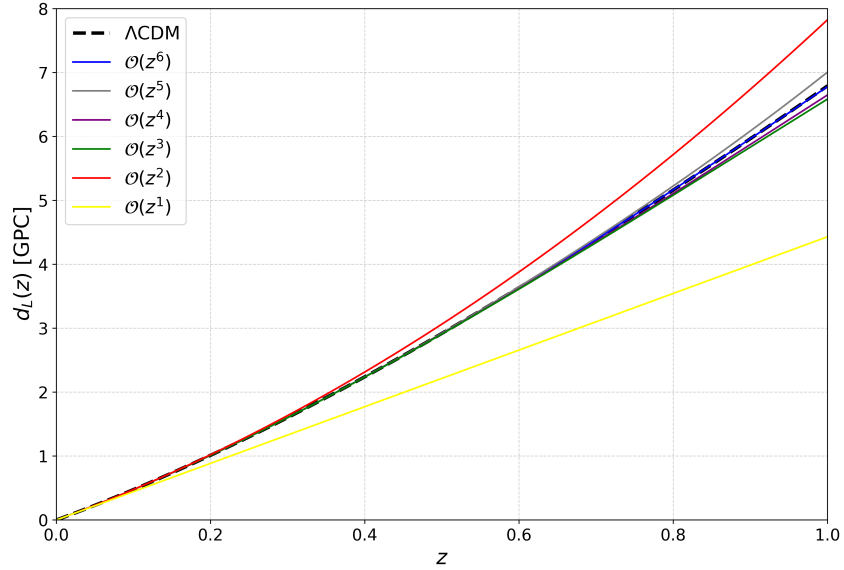


Figure 1: Luminosity distance as a function of redshift for different orders of the cosmographic series (top panel). The black dashed curve corresponds to the fiducial Λ CDM model used in the analysis. Relative difference between each cosmographic series and the fiducial model (bottom panel). The gray shaded region indicates a 1% deviation, which is reached by the third-order series at $z \approx 0.7$ (vertical dotted line).

from the fiducial model within the redshift interval $0 < z < 0.7$. Although the fourth-order and fifth-order series remain within the 1% deviation up to $z \approx 0.8$, the modest gain in the redshift range does not compensate for the introduction of additional degrees of freedom in our analysis. Therefore, according to this redshift limit, we constrain our expansions up to the third-order, with $z_{\max} = 0.7$ as the upper redshift limit for our dataset, as also adopted in previous works (see [35]). The corresponding z_{\max} values at which each cosmographic order that reaches a 1% deviation from the fiducial model are summarized in Table 2.

Order	z_{\max} for 1% deviation
$\mathcal{O}(z^1)$	0.0133
$\mathcal{O}(z^2)$	0.2047
$\mathcal{O}(z^3)$	0.6942
$\mathcal{O}(z^4)$	0.7901
$\mathcal{O}(z^5)$	0.7625
$\mathcal{O}(z^6)$	1.1827

Table 2: Redshift values at which each cosmographic expansion order reaches a maximum deviation of 1% from the fiducial Λ CDM model.

3.1 Gravitational Waves Source Distribution

The redshift distribution of coalescing sources provides a statistical description of their spatial distribution. For stellar-origin binaries, the redshift probability distribution [36] can be expressed as

$$P(z) \propto \frac{4\pi d_C^2(z)R(z)}{H(z)(1+z)}, \quad (3.2)$$

where $d_C(z) = \int_0^z H^{-1}(z')dz'$ is the comoving distance, and $R(z)$ describes the evolution of the merger rate following the cosmic star formation history (see [37]). Even though the redshift reach of gravitational wave sources can extend up to $z \approx 5$ for stellar-origin binaries, we adopt a detection limit of $z_{\max} = 0.7$ in our analysis to ensure the convergence of the cosmographic series, as explained before. The redshift distribution, given by Eq. (3.2) and with the fiducial cosmological parameters, is shown in Fig. 2.

In this work, we simulate gravitational wave data from third generation detectors, namely the Einstein Telescope and DECIGO, and the Advanced LIGO (aLIGO) is also included as a reference for current ground-based sensitivity. The interferometers considered in this work operate in the $1\text{ Hz} - 10^{-2}\text{ Hz}$ frequency band, in which binary neutron star (BNS) mergers are expected to be among the dominant bright siren sources [38, 39].

The expected number of gravitational wave detections (N_e) strongly depends on the detector sensitivity, design, and mission duration. For the Einstein Telescope, approximately 10^3 bright sirens are expected over five years of operation, with sources

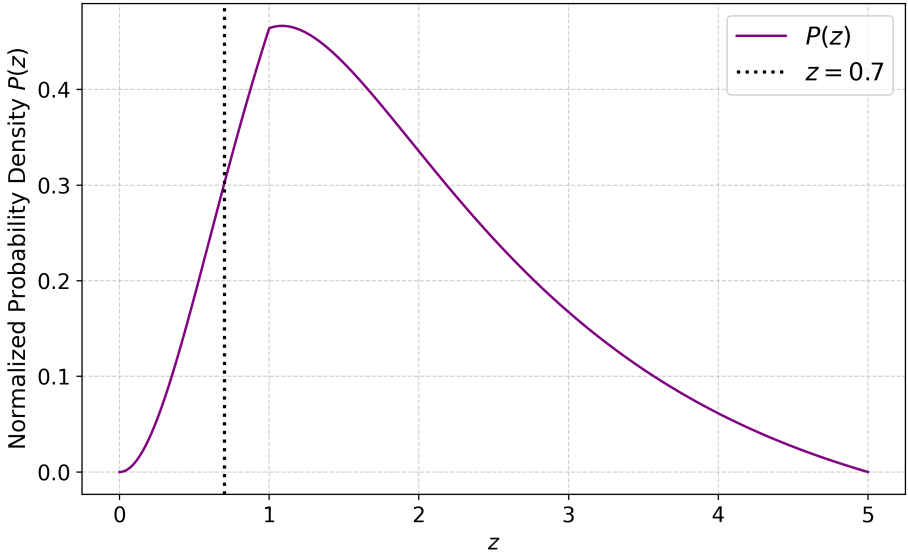


Figure 2: Normalized redshift probability density function, $P(z)$, for stellar-mass binary systems. The vertical dashed line marks the maximum redshift considered in the analysis, $z_{\max} = 0.7$.

detectable up to $z \approx 3$ [40]. DECIGO, due to its higher sensitivity, is predicted to observe around 10^4 bright sirens, reaching $z \approx 5$ [41]. In contrast, there is no clear consensus in the literature regarding the expected number of bright siren detections for Advanced LIGO, which is limited to $z \lesssim 0.2$ [42]. Therefore, we adopt a conservative estimate of one event per year [43], resulting in 10 detections over a decade of operation.

It is important to note that the detection rates quoted for each instrument refer to their full redshift range. Since our analysis is restricted to simulations up to $z_{\max} = 0.7$, the corresponding number of detectable events is lower within our redshift interval of interest.

To estimate this effective number of detections, we first generate random realizations of source redshifts following to the probability density functions defined in Eq. (3.2) over the full redshift range. We then restrict the sample to only those points within the redshift range $0 < z < 0.7$ for each detector. By performing this analysis multiple times we average the number of detections simulated and define them as N_z , which are summarized in Table 3.

Table 3: Expected number of detections (N_e) for each interferometer and the adopted number of events (N_z) within the redshift limit $z_{\max} = 0.7$.

Interferometer	N_e	N_z
Advanced LIGO	10	10
Einstein Telescope	1000	100
DECIGO	10000	800

3.2 Gravitational Waves Detection

With all the relevant information regarding the gravitational wave sources established, the next step is to simulate how these signals would be detected by ground and space-based interferometers. In the transverse-traceless (TT) gauge, the response of a detector to an incoming GW can be expressed as

$$h(t) = F_+(\theta, \phi, \psi) h_+(t) + F_\times(\theta, \phi, \psi) h_\times(t), \quad (3.3)$$

where F_+ and F_\times represent the antenna pattern functions corresponding to the two independent gravitational wave polarizations [17]. The explicit analytical forms of these functions for the aLIGO, Einstein Telescope and DECIGO detectors are presented respectively in [20, 44, 45]. The polarization components are defined as $h_+ = h_{xx} = -h_{yy}$ and $h_\times = h_{xy} = h_{yx}$.

The angular parameters (θ, ϕ) describe the sky position of the source in the detector's reference frame, while ψ denotes the polarization angle. The specific choices adopted for these angular variables in the simulations of each detector follow the prescription described in [46]. It is worth emphasizing that the antenna pattern functions depend sensitively on the geometric configuration of the interferometer, particularly on the relative orientation and the opening angle between its arms, which ultimately determine the detector's directional sensitivity.

To analyze the signal in the frequency domain, we apply the stationary phase approximation, which yields

$$\mathcal{H}(f) = \mathcal{A} f^{-7/6} e^{i\Psi(f)}, \quad (3.4)$$

where the amplitude \mathcal{A} is given by

$$\mathcal{A} = \frac{1}{d_L} \sqrt{F_+^2(1 + \cos^2 \iota)^2 + 4F_\times^2 \cos^2 \iota} \sqrt{\frac{5\pi}{96\pi}} \mathcal{M}_c^{5/6} \pi^{-7/6}. \quad (3.5)$$

Here, ι denotes the inclination angle between the orbital plane of the binary system and the observer's line of sight. The quantity \mathcal{M}_c corresponds to the observed chirp mass, defined as $\mathcal{M}_c = (1+z)M\eta^{3/5}$, where $M = m_1 + m_2$ is the total mass of the system and $\eta = \frac{m_1 m_2}{M^2}$ represents the symmetric mass ratio.

In this work, we assume uniform mass distributions for the compact objects composing the binaries [46]. For stellar-origin systems, the neutron star masses are uniformly distributed within the interval $[1, 2] M_\odot$, where M_\odot denotes the solar mass.

The phase $\Psi(f)$ in Eq. (3.4) is evaluated within the post-Newtonian framework up to 3.5PN order [47]. Within this approximation, spin effects are neglected, as their contribution to the waveform phase is subdominant for non-spinning or slowly spinning systems.

Once the amplitude and phase of the waveform are determined, the next step is to assess whether the detected strain corresponds to an actual GW signal or is merely a product of instrumental noise. A detection is claimed only when the signal-to-noise ratio (SNR) of the detector network exceeds a threshold of 8, consistent with the criterion currently adopted by the LIGO and Virgo collaborations [48].

For a network composed of N independent interferometers, the combined SNR is defined as

$$\rho = \sqrt{\sum_{i=1}^N (\rho^{(i)})^2}, \quad (3.6)$$

where $\rho^{(i)} = \sqrt{\langle \mathcal{H}^{(i)}, \mathcal{H}^{(i)} \rangle}$ denotes the SNR of the i -th detector.

The inner product used in Eq. (3.6) is computed as

$$\langle a, b \rangle \equiv 4 \int_{f_{\min}}^{f_{\max}} \frac{\tilde{a}(f)\tilde{b}^*(f) + \tilde{a}^*(f)\tilde{b}(f)}{2} \frac{df}{S_h(f)}, \quad (3.7)$$

where $\tilde{a}(f)$ and $\tilde{b}(f)$ are the Fourier transforms of the time-domain functions $a(t)$ and $b(t)$, and $S_h(f)$ is the one-sided noise power spectral density (PSD) of the detector. The frequency limits f_{\min} and f_{\max} depend on the specific interferometer configuration [46, 49]. The PSD functions for Advanced LIGO and the Einstein Telescope are taken from the official technical documentation of the respective instruments¹². Additional details on the aLIGO design sensitivity are provided in Ref. [48]. For the ET, we adopt the ET-D sensitivity configuration [50]. The DECIGO PSD is implemented following the description given in Ref. [41].

After confirming the presence of a signal via Eq. (3.6), we proceed to estimate the measurement uncertainty in the luminosity distance. The instrumental contribution to this uncertainty is evaluated within the Fisher matrix formalism [46]. As a first step, we consider a simplified estimate in which the uncertainty in the luminosity distance d_L is treated as uncorrelated with the remaining gravitational-wave parameters. Under this assumption, the instrumental error can be written as

$$\sigma_{d_L}^{\text{inst}} \simeq \sqrt{\left\langle \frac{\partial H}{\partial d_L}, \frac{\partial H}{\partial d_L} \right\rangle^{-1}}. \quad (3.8)$$

From Eqs. (3.4) and (3.5), the waveform amplitude scales as $H \propto d_L^{-1}$, leading to the well-known relation $\sigma_{d_L}^{\text{inst}} \simeq d_L/\rho$ in the absence of parameter correlations. This estimate is subsequently refined by accounting for the dominant correlation between d_L and the inclination angle ι . The inclination can modify the signal-to-noise ratio by up to a factor of two for ι in the range 0° – 90° [46]. To conservatively incorporate this effect, we rescale the uncertainty, obtaining

$$\sigma_{d_L}^{\text{inst}} \simeq \frac{2d_L}{\rho}. \quad (3.9)$$

An additional contribution to the luminosity distance uncertainty arises from weak gravitational lensing ($\sigma_{d_L}^{\text{lens}}$) [36] which can be expressed as

$$\sigma_{d_L}^{\text{lens}} = 0.05 z d_L. \quad (3.10)$$

¹<https://dcc.ligo.org/LIGO-T2000012/public>

²<https://www.et-gw.eu/index.php/etsensitivities>

We also account for the uncertainty due to peculiar velocities ($\sigma_{d_L}^{\text{PV}}$) arising from galaxy clustering and the motion of the binary barycenter [51]. This contribution is modeled as

$$\sigma_{d_L}^{\text{PV}}(z) = d_L(z) \times \left| 1 - \frac{(1+z)^2}{H(z)d_L(z)} \right| \sigma_{v,\text{gal}}, \quad (3.11)$$

where $\sigma_{v,\text{gal}}$ denotes the one-dimensional velocity dispersion of galaxies, typically taken as $\sigma_{v,\text{gal}} = 300 \text{ km s}^{-1}$, independent of redshift. The total uncertainty in the luminosity distance is then obtained by combining these contributions in quadrature:

$$\sigma_{d_L} = \sqrt{(\sigma_{d_L}^{\text{inst}})^2 + (\sigma_{d_L}^{\text{lens}})^2 + (\sigma_{d_L}^{\text{PV}})^2}. \quad (3.12)$$

Once d_L and σ_{d_L} are obtained, one may perform a Monte Carlo simulation to generate mock GW catalogues by sampling luminosity distances from a Gaussian distribution centered on the fiducial d_L values.

In Figure 3, we present a summary of the simulated data used in our analysis. The top panel shows one realization of the luminosity distance for each detector (aLIGO, ET and DECIGO), constructed following the full procedure described in this section. The bottom panel displays the fractional instrumental errors, together with the systematic contributions arising from weak lensing and peculiar velocities. As can be observed, the fractional error associated with peculiar velocities dominates at low redshifts, since small variations in local motion correspond to a significant fraction of the total luminosity distance in this regime [52]. Conversely, the lensing contribution increases with the redshift, reflecting the cumulative distortion of light paths caused by the large-scale structure of the Universe [53]. The behavior of the instrumental errors depends on the characteristics of each detector, particularly on its SNR. As shown, the next-generation interferometers exhibit significantly smaller instrumental uncertainties than the current aLIGO configuration, mainly due to their enhanced sensitivity.

3.3 Parameter Estimation

In this work, we adopt a Bayesian framework [54] to estimate the parameters $\{\theta_i\} = \{H_0, q_0, j_0\}$ given the model \mathcal{M} , represented by the cosmographic expansion in Eq. (2.5), truncated at third order. In this context, the joint posterior probability distribution of the parameters θ_i is given by

$$P(\{\theta_i\}|d, \mathcal{M}) = \frac{P(d|\{\theta_i\}, \mathcal{M}) P(\{\theta_i\}|\mathcal{M})}{P(d)}, \quad (3.13)$$

where the likelihood $P(d|\{\theta_i\}, \mathcal{M})$ is defined as

$$P(d|\{\theta_i\}, \mathcal{M}) = \exp \left[-\frac{1}{2} \sum_{i=1}^N \frac{|d_i - f_i(\{\theta_i\}, z_i)|^2}{\sigma_i^2} \right], \quad (3.14)$$

with N being the number of detections, d_i the observed data with uncertainty σ_i , and $f_i(\{\theta_i\}, z_i)$ the model prediction, corresponding to the third-order truncation of Eq. (2.5). The priors on H_0 , q_0 , and j_0 are assumed to be uniform within the ranges

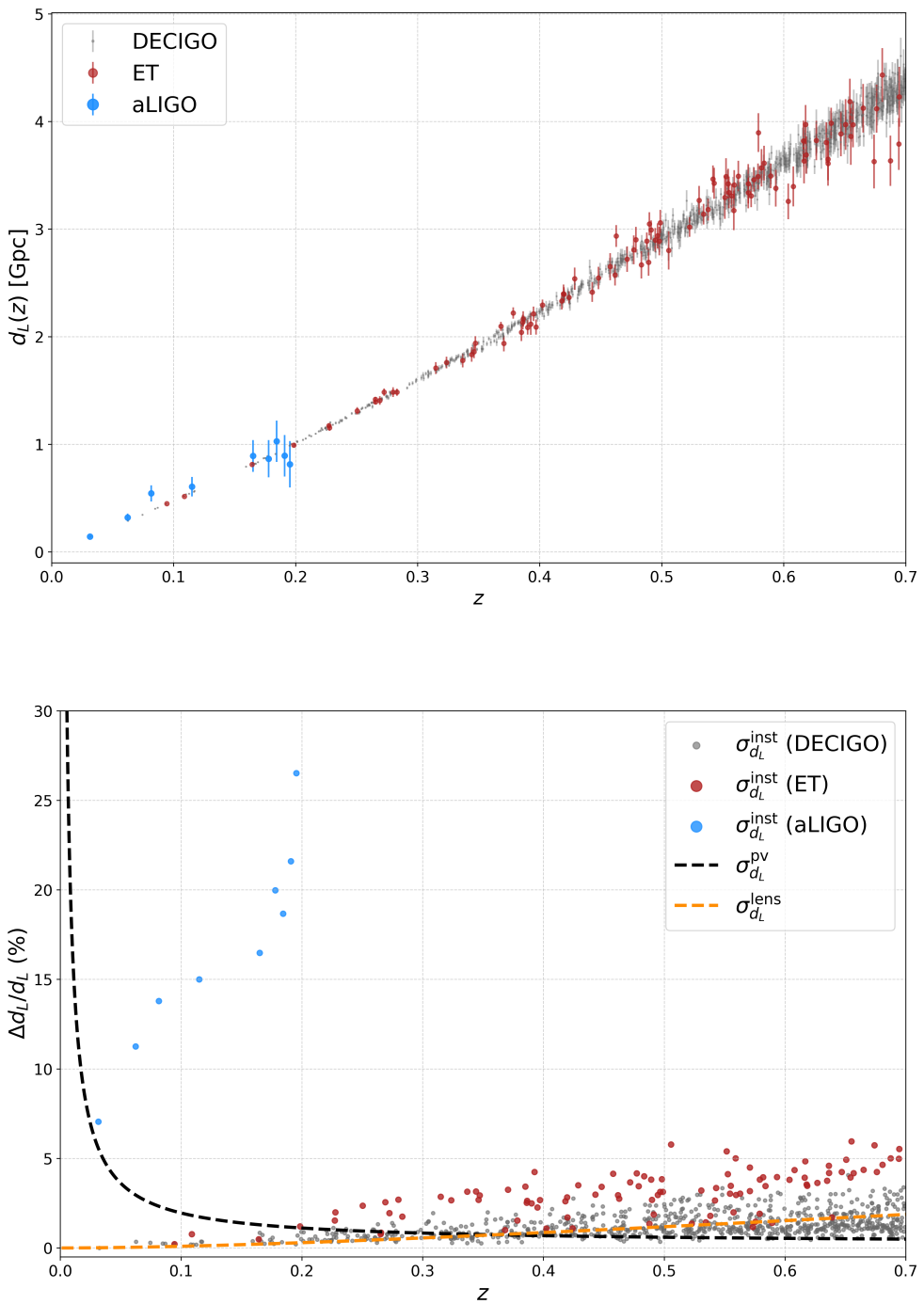


Figure 3: Simulated catalogs of luminosity distance for each interferometer (DECIGO, ET and aLIGO), with the number of detections set to N_z and a maximum redshift of $z_{\text{max}} \simeq 0.7$ (top panel). Fractional uncertainties on the luminosity distance, where the points correspond to the instrumental errors extracted from the simulated catalogs, and the dashed and solid curves represent the systematic contributions from weak lensing and peculiar velocities, respectively, expressed as $\Delta d_L/d_L \times 100\%$ (bottom panel).

$[54, 81] \text{ km s}^{-1} \text{ Mpc}^{-1}$, $[-1, 0]$, and $[-1, 3]$, respectively, chosen to encompass current observational constraints while remaining sufficiently broad to avoid informative priors. We note that the uncertainty in the redshift is neglected, consistently with the assumption of an electromagnetic counterpart to the gravitational wave signal, which allows for the unambiguous identification of the host galaxy.

4 Results

In this section we apply the previously described methodology in order to investigate what is the impact on the cosmographic parameters due to the forecast of different observational regimes of gravitational wave detectors. We focus on two complementary dependences: the signal-to-noise ratio (SNR) and the number of detections (N_z), as described in the next sections. This procedure aims to assess how the future catalogues with configurations beyond the current ones enhances the precision of H_0 , q_0 , and j_0 , providing insights into the constraining power of future high-sensitivity observatories.

For each analysis we performed 50 independent realizations and estimate the average of the mean values and the average of the standard deviations across all realizations. The posterior distributions of H_0 , q_0 , and j_0 are obtained via a Markov Chain Monte Carlo (MCMC) approach using `emcee` [55]. A comprehensive summary of the adopted SNR intervals, the number of events, and the MCMC-derived cosmographic results is presented in Appendix A in Tables 4, 5, and 6. In addition, Figures 5 and 6 illustrate the behavior of the parameter uncertainties as functions of both SNR and N for all interferometers analyzed.

4.1 SNR Analysis

Regarding the first analysis, we generate simulated catalogs for different SNR values and the corresponding number of events N_z distributed over the redshift range $z \in [0, 0.7]$. For each interferometer, the minimum and maximum SNR values are defined according to its sensitivity, and this interval is divided into bins. Simulations are then performed for each bin, yielding different values of N_z . For each event, up to 500 trials of source-parameter combinations are allowed to satisfy the target SNR. If no successful combination is found, the simulation proceeds to the next redshift, which naturally leads to a non-constant number of events across the SNR bins. The average number of events obtained from 50 realizations for each bin and for each interferometer, namely aLIGO (blue), the ET (red) and DECIGO (green), is shown in Fig. 4. In the next step, a MCMC analysis is carried out to evaluate the variation of the uncertainties of the cosmographic parameters, as presented in Fig. 5. In this figure, the points correspond to the mean SNR value of each bin, and the color coding follows the same convention adopted in Fig. 4.

As shown in Fig. 5, the uncertainty in the Hubble constant (σ_{H_0}) for aLIGO attains its tightest constraint in the interval $\text{SNR} \in [40, 44]$, reaching a precision of $\sigma_{H_0} = 1.395 \text{ km s}^{-1} \text{ Mpc}^{-1}$, which is comparable to that obtained by the Einstein Telescope at the high-SNR end of its distribution. The latter exhibits a more

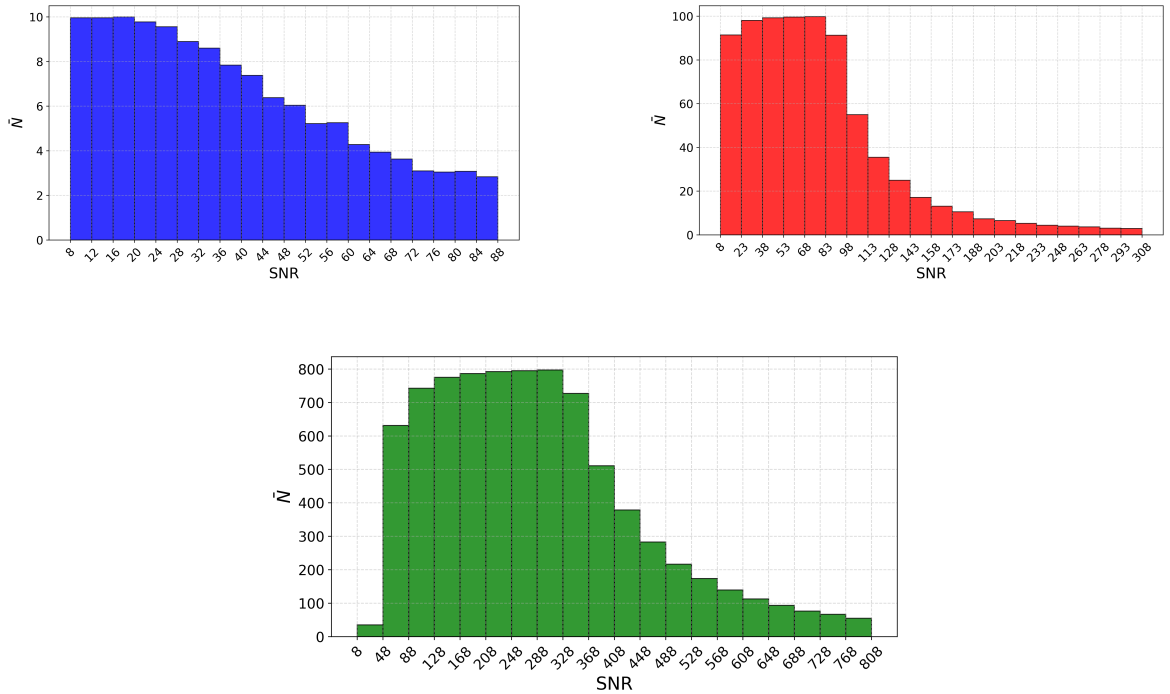


Figure 4: Mean number of simulated events, \bar{N} , per signal-to-noise ratio (SNR) interval for each interferometer, averaged over 50 independent realizations. The top-left and top-right panels correspond to aLIGO and the Einstein Telescope, respectively, while the bottom panel shows the results for DECIGO.

stable trend, achieving its best constraint in the range $\text{SNR} \in [128, 143]$, where $\sigma_{H_0} = 1.115 \text{ km s}^{-1} \text{ Mpc}^{-1}$. In contrast, DECIGO displays a different behavior and reaches its tightest constraint in the interval $\text{SNR} \in [288, 328]$, with an uncertainty of $\sigma_{H_0} = 0.315 \text{ km s}^{-1} \text{ Mpc}^{-1}$, thus providing the most precise determination of H_0 among the detectors analyzed. However, DECIGO also yields the poorest H_0 constraint in the lowest SNR bin ($\text{SNR} \in [8, 48]$), probably due to the rarity of low-SNR detections within the adopted redshift range.

Following toward higher-order parameters, the middle panel of Figure 5 shows the uncertainty in the deceleration parameter (σ_{q_0}). Since q_0 enters the cosmographic expansion of the luminosity distance at second order, its contribution scales as z^2 , making its determination intrinsically dependent on access to higher-redshift events, in contrast to H_0 , which is primarily constrained by nearby sources. As a result, aLIGO, whose detections are mostly limited to $z \lesssim 0.2$, shows only a weak improvement with increasing SNR, achieving its best constraint at $\text{SNR} \in [20, 24]$ with $\sigma_{q_0} = 0.3335$. The Einstein Telescope, benefiting from a broader redshift coverage and a larger event sample, exhibits a more structured behavior, with a clear minimum at intermediate SNR values. Its tightest constraints are reached in the range $\text{SNR} \in [158, 173] - [173, 188]$, where $\sigma_{q_0} = 0.2000$. At high SNR, DECIGO provides the most stringent determination of q_0 , reaching $\sigma_{q_0} = 0.0535$ in the range

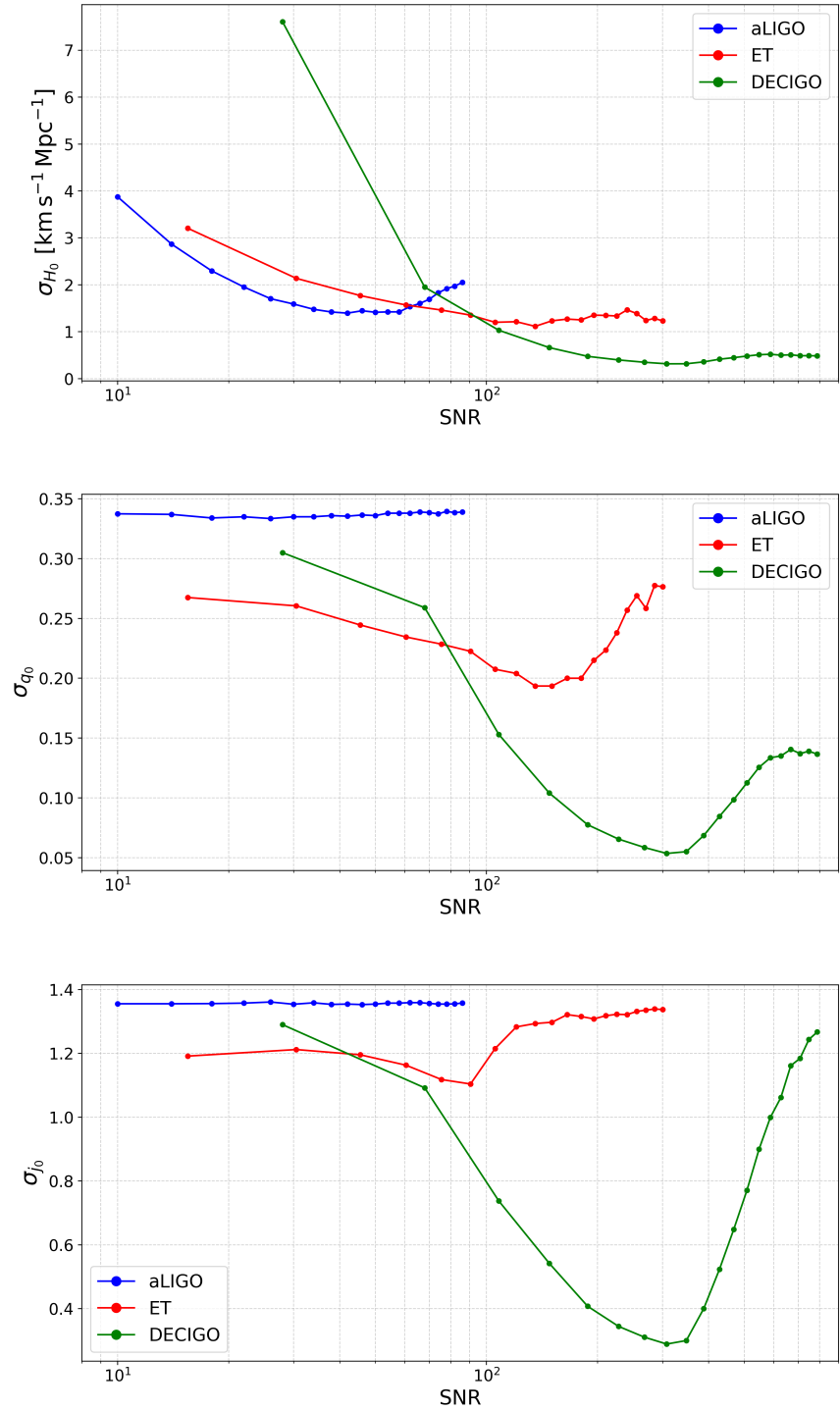


Figure 5: Uncertainties, σ , of the cosmographic parameters H_0 , q_0 , and j_0 as functions of the signal-to-noise ratio (SNR). The top, middle, and bottom panels correspond to H_0 , q_0 , and j_0 , respectively. The curves show the results obtained for the different interferometers considered in this analysis.

$\text{SNR} \in [288, 328]$, reflecting its ability to accumulate a large number of detections at higher redshifts where sensitivity to q_0 is maximized.

The bottom panel of Figure 5 displays the uncertainty in the jerk parameter (σ_{j_0}) as a function of the signal-to-noise ratio. Due to the same order dependence of the other cosmographic parameters, the aLIGO shows an almost flat behavior across the SNR range, with its best constraint obtained at $\text{SNR} \in [28, 32]$, where $\sigma_{j_0} = 1.354$, while the Einstein Telescope achieves its tightest constraint in the interval $\text{SNR} \in [83, 98]$ with $\sigma_{j_0} = 1.104$. At high SNR, DECIGO provides the most stringent determination of the jerk parameter, reaching $\sigma_{j_0} = 0.289$ in the interval $\text{SNR} \in [288, 328]$, reflecting its ability to probe a large number of high-redshift sources where sensitivity to j_0 is maximized.

4.2 N Analysis

In the second part of the analysis, the number of events is systematically increased from the values presented in Table 3 up to optimistic detection scenarios for each interferometer.

The top panel of Fig. 6 illustrates how the uncertainty in the Hubble constant, σ_{H_0} , systematically decreases as the number of detected events increases for all interferometers, as expected for progressively more optimistic detection scenarios. In the case of aLIGO, σ_{H_0} improves from $2.190 \text{ km s}^{-1} \text{ Mpc}^{-1}$ at $N = 10$ to $0.765 \text{ km s}^{-1} \text{ Mpc}^{-1}$ at $N = 100$, with a precision already comparable to that of the Einstein Telescope at $N = 60$. The Einstein Telescope itself yields significantly tighter constraints, reaching $\sigma_{H_0} = 0.430 \text{ km s}^{-1} \text{ Mpc}^{-1}$ in its most optimistic configuration ($N = 550$). Nevertheless, within the range explored here, DECIGO outperforms all other detectors, providing the most stringent measurements of H_0 , from $\sigma_{H_0} = 0.300 \text{ km s}^{-1} \text{ Mpc}^{-1}$ at $N = 800$ down to $0.170 \text{ km s}^{-1} \text{ Mpc}^{-1}$ for $N = 2600$.

Moving to higher-order cosmographic parameters, the middle panel of Fig. 6 presents the constraints on the deceleration parameter, σ_{q_0} , which also improve with increasing event numbers. However, in contrast to H_0 , aLIGO shows a much weaker gain in precision, reflecting the limited sensitivity of q_0 to low-redshift observations. Even in the most optimistic aLIGO scenario ($N = 100$), the uncertainty remains relatively large, $\sigma_{q_0} = 0.3140$. The Einstein Telescope performs considerably better, already achieving $\sigma_{q_0} = 0.1550$ at $N = 100$ and improving to 0.0915 at $N = 550$, although it still does not reach the precision attainable with DECIGO. As in the case of H_0 , DECIGO delivers the tightest constraints, reducing σ_{q_0} from 0.0545 at $N = 800$ to 0.0300 in the most optimistic configuration.

An even clearer separation among the interferometers is found for the jerk parameter, as shown in the bottom panel of Fig. 6. Due to its strong dependence on redshift, the σ_{j_0} for aLIGO remains nearly constant, changing from 1.3475 at $N = 10$ to 1.3520 at $N = 100$. In contrast, the Einstein Telescope shows a clear improvement with increasing statistics, with σ_{j_0} decreasing from 1.0335 in the baseline case ($N = 100$) to 0.5635 for $N = 550$, although it again falls short of the performance of DECIGO. Consistently across all parameters, DECIGO provides the most stringent constraints,

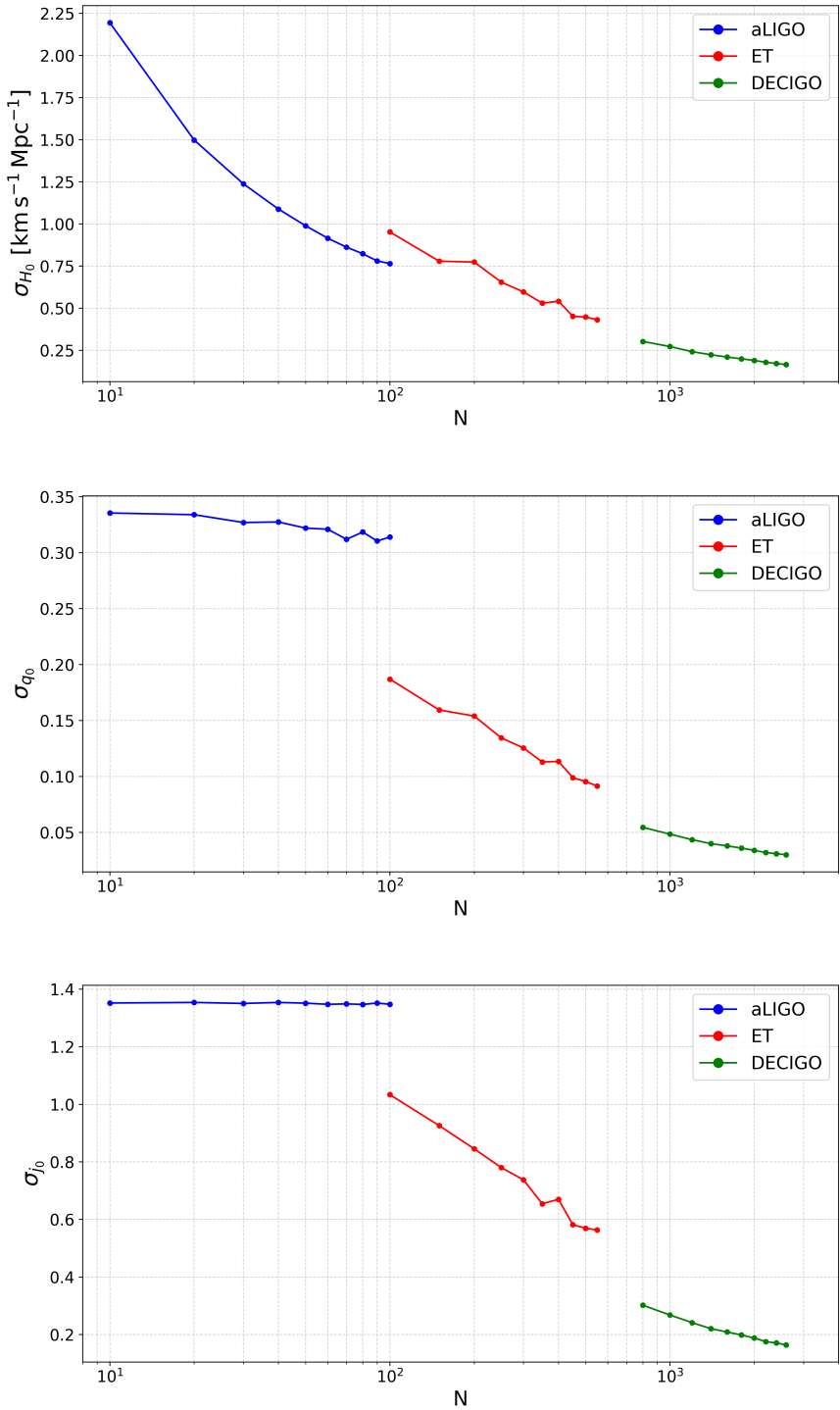


Figure 6: Uncertainties, σ , of the cosmographic parameters H_0 , q_0 , and j_0 as functions of the number of detections, N . The top, middle, and bottom panels correspond to H_0 , q_0 , and j_0 , respectively. The curves show the results obtained for the different interferometers considered in this analysis: aLIGO, the Einstein Telescope, and DECIGO.

achieving $\sigma_{j_0} = 0.3020$ already at $N = 800$ and reaching 0.1640 in the most optimistic scenario with $N = 2600$.

5 Conclusions

In the present paper we investigated the capability of future gravitational wave observations with both current detectors, such as Advanced LIGO, as well as next-generation interferometers, including the Einstein Telescope and DECIGO, to constrain the parameters of the cosmographic expansion like the Hubble constant, deceleration and jerk parameters. It is well known that truncated cosmographic series are not expected to accurately describe the cosmic expansion beyond redshifts of order unity. In this work, we demonstrated that truncation at third order, combined with a maximum redshift of $z_{\max} = 0.70$, provides a reliable and self-consistent cosmographic framework. The simulated catalogs assume the detection of electromagnetic counterparts, ensuring accurate redshift determination, with sources observed up to z_{\max} . We further examined how the uncertainties in the cosmographic parameters depend on the signal-to-noise ratio of the detections and on increasingly optimistic scenarios for the total number of observed events.

The accuracy achieved by gravitational wave standard sirens, summarized in Tables 4, 5 and 6, has direct implications for the Hubble tension [56–59]. For Advanced LIGO, constraints on H_0 at the few-percent level are not expected to fully resolve the discrepancy between early and late Universe determinations; nevertheless, they already provide an independent and calibration-free measurement capable of alleviating the tension, particularly when optimistic assumptions on the total number of detected events are considered. A qualitatively different constraining power is attained by next-generation interferometers. The Einstein Telescope consistently operates in the percent-precision regime, approaching sub-percent accuracy as the event sample grows, thereby entering the domain where meaningful discrimination among competing cosmological scenarios becomes possible. This capability is further strengthened by DECIGO, which delivers sub-percent constraints on H_0 even under conservative signal-to-noise conditions and reaches accuracies well below the percent level for large event numbers, firmly placing space-based gravitational wave observations within the framework of high-precision cosmology.

On the other hand, the constraining power of gravitational-wave observations on higher-order cosmographic parameters in our results presents a qualitatively different picture. While only DECIGO is able to constrain the deceleration parameter q_0 with a precision better than 10%, a similar pattern is observed for the jerk parameter j_0 . Advanced LIGO and the Einstein Telescope yield uncertainty of order unity, indicating limited sensitivity to deviations from the standard Λ CDM expectation $j_0 = 1$. In contrast, DECIGO achieves substantially tighter bounds, reaching a few tens of percent precision in the signal-to-noise-based analysis and improving further under optimistic event-number scenarios. This level of accuracy is particularly relevant in light of recent results from DESI [60, 61], which probe the expansion history through baryon acoustic oscillations and have reported indications of possible departures from the cosmological

constant. The ability of DECIGO to access j_0 with meaningful precision suggests that future gravitational wave observations may provide a complementary and calibration-free avenue to investigate the dynamical nature of dark energy.

Our analysis also highlights an important limitation associated with the redshift reach of Advanced LIGO. Due to its restricted sensitivity to sources at $z \lesssim 0.2$, improvements in the precision of higher-order cosmographic parameters, such as q_0 and j_0 , remain marginal even under optimistic assumptions for the total number of detected events, resulting in an almost flat behavior of the corresponding uncertainties. This behavior can be understood by examining the derivatives of the Hubble expansion rate $H(z)$ with respect to q_0 and j_0 , whose sensitivity increases significantly only at higher redshifts. As discussed in previous studies (see, e.g., Ref. [35]), redshifts $z \gtrsim 0.4$ are required to meaningfully probe these higher-order terms, in full agreement with our findings.

In summary, we have shown that gravitational wave standard sirens provide a robust and versatile framework for cosmographic studies in the low-redshift Universe. Second-generation detectors already play a relevant role by delivering independent measurements of the Hubble constant that can alleviate the current tension, while third-generation and space-based interferometers extend this approach into the regime of high-precision cosmology. In particular, the combination of percent-level constraints on H_0 and meaningful sensitivity to higher-order parameters achieved by DECIGO highlights the potential of future gravitational wave observations to go beyond consistency checks and actively probe the physics driving cosmic acceleration. As gravitational wave catalogs continue to grow in size and sensitivity, cosmography with standard sirens is poised to become a powerful complementary tool to traditional electromagnetic surveys in shaping our understanding of the expansion history of the Universe.

References

- [1] B. P. e. a. Abbott, *Astrophys. J. Lett.* **848**, L12 (2017).
- [2] B. P. Abbott *et al.* (LIGO Scientific, Virgo), *Phys. Rev. Lett.* **116**, 061102 (2016), [arXiv:1602.03837 \[gr-qc\]](https://arxiv.org/abs/1602.03837) .
- [3] J. Aasi *et al.* (LIGO Scientific), *Class. Quant. Grav.* **32**, 074001 (2015), [arXiv:1411.4547 \[gr-qc\]](https://arxiv.org/abs/1411.4547) .
- [4] F. Acernese *et al.* (VIRGO), *Class. Quant. Grav.* **32**, 024001 (2015), [arXiv:1408.3978 \[gr-qc\]](https://arxiv.org/abs/1408.3978) .
- [5] K. Somiya (KAGRA), *Class. Quant. Grav.* **29**, 124007 (2012), [arXiv:1111.7185 \[gr-qc\]](https://arxiv.org/abs/1111.7185) .
- [6] A. G. Abac *et al.* (LIGO Scientific, VIRGO, KAGRA), (2025), [arXiv:2508.18079 \[gr-qc\]](https://arxiv.org/abs/2508.18079) .
- [7] M. Punturo *et al.*, *Class. Quant. Grav.* **27**, 194002 (2010).
- [8] S. Kawamura *et al.*, *Class. Quant. Grav.* **23**, S125 (2006).

[9] B. P. Abbott *et al.* (LIGO Scientific, Virgo), *Phys. Rev. Lett.* **119**, 161101 (2017), [arXiv:1710.05832 \[gr-qc\]](#) .

[10] B. F. Schutz, *Nature* **323**, 310 (1986).

[11] D. Branch and G. A. Tammann, *Ann. Rev. Astron. Astrophys.* **30**, 359 (1992).

[12] B. P. Abbott *et al.* (LIGO Scientific, Virgo), *Astrophys. J. Lett.* **892**, L3 (2020), [arXiv:2001.01761 \[astro-ph.HE\]](#) .

[13] R. Abbott *et al.* (LIGO Scientific, KAGRA, VIRGO), *Astrophys. J. Lett.* **915**, L5 (2021), [arXiv:2106.15163 \[astro-ph.HE\]](#) .

[14] B. P. Abbott *et al.* (LIGO Scientific, Virgo, Fermi-GBM, INTEGRAL), *Astrophys. J. Lett.* **848**, L13 (2017), [arXiv:1710.05834 \[astro-ph.HE\]](#) .

[15] D. E. Holz and S. A. Hughes, *Astrophys. J.* **629**, 15 (2005), [arXiv:astro-ph/0504616](#) .

[16] B. P. Abbott *et al.* (LIGO Scientific, Virgo, 1M2H, Dark Energy Camera GW-E, DES, DLT40, Las Cumbres Observatory, VINROUGE, MASTER), *Nature* **551**, 85 (2017), [arXiv:1710.05835 \[astro-ph.CO\]](#) .

[17] B. S. Sathyaprakash and B. F. Schutz, *Living Rev. Rel.* **12**, 2 (2009), [arXiv:0903.0338 \[gr-qc\]](#) .

[18] X.-N. Zhang, L.-F. Wang, J.-F. Zhang, and X. Zhang, *Phys. Rev. D* **99**, 063510 (2019), [arXiv:1804.08379 \[astro-ph.CO\]](#) .

[19] L.-F. Wang, S.-J. Jin, J.-F. Zhang, and X. Zhang, *Sci. China Phys. Mech. Astron.* **65**, 210411 (2022), [arXiv:2101.11882 \[gr-qc\]](#) .

[20] T. Yang, *JCAP* **05**, 044 (2021), [arXiv:2103.01923 \[astro-ph.CO\]](#) .

[21] A. Finke, S. Foffa, F. Iacobelli, M. Maggiore, and M. Mancarella, *JCAP* **08**, 026 (2021), [arXiv:2101.12660 \[astro-ph.CO\]](#) .

[22] G. Sala, A. Cuoco, J. Lesgourgues, K.-R. Revis, L. Valbusa Dall'Armi, and S. Casas, (2025), [arXiv:2510.08699 \[astro-ph.CO\]](#) .

[23] S. Mastrogiiovanni, D. Laghi, R. Gray, G. C. Santoro, A. Ghosh, C. Karathanasis, K. Leyde, D. A. Steer, S. Perries, and G. Pierra, *Phys. Rev. D* **108**, 042002 (2023), [arXiv:2305.10488 \[astro-ph.CO\]](#) .

[24] S. Weinberg, *Gravitation & Cosmology: Principles and Applications of the General Theory of Relativity* (John Wiley and Sons, New York, 1972).

[25] M. Visser, *Gen. Rel. Grav.* **37**, 1541 (2005), [arXiv:gr-qc/0411131](#) .

[26] M.-J. Zhang, H. Li, and J.-Q. Xia, *Eur. Phys. J. C* **77**, 434 (2017), [arXiv:1601.01758 \[astro-ph.CO\]](#) .

[27] C. Cattoen and M. Visser, *Class. Quant. Grav.* **24**, 5985 (2007), [arXiv:0710.1887 \[gr-qc\]](#) .

[28] R. Lazkoz, J. Alcaniz, C. Escamilla-Rivera, V. Salzano, and I. Sendra, *JCAP* **12**, 005 (2013), [arXiv:1311.6817 \[astro-ph.CO\]](#) .

[29] C. Gruber and O. Luongo, *Phys. Rev. D* **89**, 103506 (2014), [arXiv:1309.3215 \[gr-qc\]](#) .

[30] A. Shafieloo, *JCAP* **05**, 024 (2012), arXiv:1202.4808 [astro-ph.CO] .

[31] J. P. Hu and F. Y. Wang, *Astron. Astrophys.* **661**, A71 (2022), arXiv:2202.09075 [astro-ph.CO] .

[32] N. Aghanim *et al.* (Planck), *Astron. Astrophys.* **641**, A6 (2020), [Erratum: *Astron. Astrophys.* 652, C4 (2021)], arXiv:1807.06209 [astro-ph.CO] .

[33] A. G. Riess *et al.*, *Astrophys. J. Lett.* **934**, L7 (2022), arXiv:2112.04510 [astro-ph.CO] .

[34] A. Aviles, C. Gruber, O. Luongo, and H. Quevedo, *Phys. Rev. D* **86**, 123516 (2012), arXiv:1204.2007 [astro-ph.CO] .

[35] J. M. S. de Souza, R. Sturani, and J. Alcaniz, *JCAP* **03**, 025 (2022), arXiv:2110.13316 [gr-qc] .

[36] W. Zhao, C. Van Den Broeck, D. Baskaran, and T. G. F. Li, *Phys. Rev. D* **83**, 023005 (2011), arXiv:1009.0206 [astro-ph.CO] .

[37] R. Schneider, V. Ferrari, S. Matarrese, and S. F. Portegies Zwart, *Mon. Not. Roy. Astron. Soc.* **324**, 797 (2001), arXiv:astro-ph/0002055 .

[38] B. Patricelli, M. G. Bernardini, M. Mapelli, P. D’Avanzo, F. Santoliquido, G. Cella, M. Razzano, and E. Cuoco, *Mon. Not. Roy. Astron. Soc.* **513**, 4159 (2022), [Erratum: *Mon. Not. Roy. Astron. Soc.* 514, 3395 (2022)], arXiv:2204.12504 [astro-ph.HE] .

[39] C. Liu, Y. Kang, and L. Shao, *Astrophys. J.* **934**, 84 (2022), arXiv:2204.06161 [astro-ph.HE] .

[40] E. e. a. Barausse, *Einstein Telescope Design Report Update 2020*, Tech. Rep. ET-0007B-20 (Einstein Telescope Collaboration, 2020).

[41] T. Liu, S. Cao, M. Biesiada, Y. Zhang, and J. Wang, *Astrophys. J. Lett.* **965**, L11 (2024), arXiv:2404.07419 [astro-ph.CO] .

[42] M. Lagos, M. Fishbach, P. Landry, and D. E. Holz, *Phys. Rev. D* **99**, 083504 (2019), arXiv:1901.03321 [astro-ph.CO] .

[43] B. F. Schutz, *Phil. Trans. Roy. Soc. Lond. A* **376**, 20170279 (2018), arXiv:1804.06308 [astro-ph.IM] .

[44] M. Califano, I. de Martino, D. Vernieri, and S. Capozziello, *Mon. Not. Roy. Astron. Soc.* **518**, 3372 (2022), arXiv:2205.11221 [astro-ph.CO] .

[45] K. Yagi and N. Seto, *Phys. Rev. D* **83**, 044011 (2011), [Erratum: *Phys. Rev. D* 95, 109901 (2017)], arXiv:1101.3940 [astro-ph.CO] .

[46] R.-G. Cai, T.-B. Liu, X.-W. Liu, S.-J. Wang, and T. Yang, *Phys. Rev. D* **97**, 103005 (2018), arXiv:1712.00952 [astro-ph.CO] .

[47] A. Nishizawa, A. Taruya, and S. Saito, *Phys. Rev. D* **83**, 084045 (2011).

[48] B. P. Abbott *et al.* (KAGRA, LIGO Scientific, Virgo), *Living Rev. Rel.* **19**, 1 (2016), arXiv:1304.0670 [gr-qc] .

[49] L. Yang, H.-Y. Wan, T.-J. Zhang, and T. Yanke, (2017), arXiv:1703.07923 [astro-ph.CO] .

[50] S. Hild *et al.*, *Class. Quant. Grav.* **28**, 094013 (2011), arXiv:1012.0908 [gr-qc] .

- [51] C. Gordon, K. Land, and A. Slosar, *Phys. Rev. Lett.* **99**, 081301 (2007), [arXiv:0705.1718 \[astro-ph\]](https://arxiv.org/abs/0705.1718) .
- [52] C. Blake and R. J. Turner, (2025), [arXiv:2509.03101 \[astro-ph.CO\]](https://arxiv.org/abs/2509.03101) .
- [53] S. Canevarolo and N. E. Chisari, *Mon. Not. Roy. Astron. Soc.* **533**, 36 (2024), [arXiv:2310.12764 \[astro-ph.CO\]](https://arxiv.org/abs/2310.12764) .
- [54] R. Trotta (2017) [arXiv:1701.01467 \[astro-ph.CO\]](https://arxiv.org/abs/1701.01467) .
- [55] D. Foreman-Mackey, D. W. Hogg, D. Lang, and J. Goodman, *Publications of the Astronomical Society of the Pacific* **125**, 306–312 (2013).
- [56] E. Di Valentino, O. Mena, S. Pan, L. Visinelli, W. Yang, A. Melchiorri, D. F. Mota, A. G. Riess, and J. Silk, *Class. Quant. Grav.* **38**, 153001 (2021), [arXiv:2103.01183 \[astro-ph.CO\]](https://arxiv.org/abs/2103.01183) .
- [57] J.-P. Hu and F.-Y. Wang, *Universe* **9**, 94 (2023), [arXiv:2302.05709 \[astro-ph.CO\]](https://arxiv.org/abs/2302.05709) .
- [58] S. Capozziello, G. Sarracino, and G. De Somma, *Universe* **10**, 140 (2024), [arXiv:2403.12796 \[gr-qc\]](https://arxiv.org/abs/2403.12796) .
- [59] L. Kraiselburd, C. Pigozzo, S. J. Landau, and J. Alcaniz, (2025), [arXiv:2504.06831 \[astro-ph.CO\]](https://arxiv.org/abs/2504.06831) .
- [60] M. Abdul Karim *et al.* (DESI), *Phys. Rev. D* **112**, 083515 (2025), [arXiv:2503.14738 \[astro-ph.CO\]](https://arxiv.org/abs/2503.14738) .
- [61] G. Rodrigues, R. de Souza, and J. Alcaniz, *Phys. Rev. D* **112**, 103519 (2025), [arXiv:2506.22373 \[astro-ph.CO\]](https://arxiv.org/abs/2506.22373) .

A Numerical Results for the SNR-based and N Analysis

SNR interval / N	H_0 (Km/s/Mpc)	q_0	j_0	σ_{H_0}/H_0 (%)	$\sigma_{q_0}/ q_0 $ (%)	σ_{j_0}/j_0 (%)
SNR Intervals						
[8,12]	$68.02^{+4.03}_{-3.72}$	$-0.508^{+0.341}_{-0.334}$	$0.993^{+1.357}_{-1.354}$	5.7	66.5	136.6
[12,16]	$67.72^{+2.98}_{-2.75}$	$-0.508^{+0.342}_{-0.332}$	$1.003^{+1.353}_{-1.358}$	4.2	66.6	135.5
[16,20]	$67.69^{+2.37}_{-2.23}$	$-0.510^{+0.338}_{-0.330}$	$0.993^{+1.359}_{-1.353}$	3.4	65.4	136.9
[20,24]	$67.60^{+2.00}_{-1.91}$	$-0.501^{+0.336}_{-0.334}$	$1.003^{+1.356}_{-1.359}$	2.9	66.8	135.4
[24,28]	$67.35^{+1.74}_{-1.66}$	$-0.495^{+0.332}_{-0.334}$	$0.999^{+1.364}_{-1.358}$	2.5	67.2	136.2
[28,32]	$67.69^{+1.62}_{-1.56}$	$-0.507^{+0.338}_{-0.332}$	$0.993^{+1.356}_{-1.352}$	2.3	66.0	136.7
[32,36]	$67.93^{+1.51}_{-1.45}$	$-0.508^{+0.339}_{-0.331}$	$1.000^{+1.359}_{-1.358}$	2.2	66.1	135.9
[36,40]	$67.68^{+1.45}_{-1.39}$	$-0.504^{+0.338}_{-0.334}$	$0.996^{+1.357}_{-1.350}$	2.1	66.7	136.1
[40,44]	$68.07^{+1.42}_{-1.37}$	$-0.505^{+0.339}_{-0.332}$	$0.999^{+1.353}_{-1.356}$	2.1	66.4	135.5
[44,48]	$68.32^{+1.47}_{-1.42}$	$-0.519^{+0.345}_{-0.328}$	$0.983^{+1.362}_{-1.344}$	2.1	64.9	137.2
[48,52]	$67.67^{+1.44}_{-1.39}$	$-0.507^{+0.333}_{-0.333}$	$1.001^{+1.357}_{-1.357}$	2.1	65.7	135.7
[52,56]	$67.64^{+1.45}_{-1.39}$	$-0.496^{+0.336}_{-0.340}$	$0.991^{+1.361}_{-1.354}$	2.1	68.1	136.7
[56,60]	$67.62^{+1.45}_{-1.40}$	$-0.503^{+0.339}_{-0.337}$	$0.994^{+1.360}_{-1.355}$	2.1	67.1	136.4
[60,64]	$67.27^{+1.57}_{-1.50}$	$-0.503^{+0.340}_{-0.336}$	$0.999^{+1.358}_{-1.360}$	2.3	67.3	135.9
[64,68]	$67.73^{+1.64}_{-1.56}$	$-0.503^{+0.341}_{-0.337}$	$0.993^{+1.364}_{-1.354}$	2.4	67.3	136.8
[68,72]	$67.76^{+1.65}_{-1.74}$	$-0.506^{+0.341}_{-0.336}$	$1.010^{+1.361}_{-1.349}$	2.5	66.9	135.3
[72,76]	$68.33^{+1.88}_{-1.77}$	$-0.500^{+0.337}_{-0.338}$	$1.011^{+1.355}_{-1.353}$	2.7	67.5	134.8
[76,80]	$68.18^{+1.96}_{-1.87}$	$-0.505^{+0.340}_{-0.337}$	$0.998^{+1.355}_{-1.356}$	2.8	66.9	135.7
[80,84]	$67.81^{+2.03}_{-1.92}$	$-0.501^{+0.343}_{-0.337}$	$1.005^{+1.349}_{-1.354}$	2.9	67.9	134.6
[84,88]	$67.97^{+2.11}_{-1.99}$	$-0.506^{+0.342}_{-0.336}$	$1.003^{+1.356}_{-1.360}$	3.0	66.9	135.7
N						
10	$67.74^{+2.25}_{-2.13}$	$-0.506^{+0.339}_{-0.332}$	$1.009^{+1.342}_{-1.362}$	3.2	66.4	134.8
20	$67.79^{+1.52}_{-1.47}$	$-0.498^{+0.334}_{-0.334}$	$1.013^{+1.346}_{-1.362}$	2.2	67.1	134.5
30	$67.43^{+1.26}_{-1.21}$	$-0.524^{+0.337}_{-0.317}$	$0.979^{+1.346}_{-1.342}$	1.8	62.8	137.1
40	$67.69^{+1.10}_{-1.08}$	$-0.532^{+0.340}_{-0.315}$	$0.966^{+1.374}_{-1.334}$	1.6	61.1	140.3
50	$67.56^{+1.01}_{-0.97}$	$-0.511^{+0.327}_{-0.317}$	$0.983^{+1.359}_{-1.344}$	1.5	63.1	137.0
60	$67.62^{+0.92}_{-0.91}$	$-0.493^{+0.320}_{-0.322}$	$1.003^{+1.348}_{-1.347}$	1.4	64.9	134.4
70	$67.61^{+0.88}_{-0.85}$	$-0.481^{+0.304}_{-0.320}$	$1.010^{+1.345}_{-1.353}$	1.3	64.9	133.6
80	$67.51^{+0.83}_{-0.82}$	$-0.519^{+0.326}_{-0.311}$	$0.980^{+1.354}_{-1.340}$	1.2	61.7	137.5
90	$67.71^{+0.79}_{-0.77}$	$-0.482^{+0.306}_{-0.315}$	$1.023^{+1.345}_{-1.359}$	1.2	64.5	132.6
100	$67.66^{+0.77}_{-0.76}$	$-0.497^{+0.311}_{-0.317}$	$0.998^{+1.350}_{-1.345}$	1.1	63.2	135.0

Table 4: Cosmographic parameter estimates for the aLIGO interferometer as a function of the signal-to-noise ratio and the number of detected events.

SNR interval / N	H_0 (Km/s/Mpc)	q_0	j_0	σ_{H_0}/H_0 (%)	$\sigma_{q_0}/ q_0 $ (%)	σ_{j_0}/j_0 (%)
SNR Intervals						
[8,23]	$67.47^{+3.33}_{-3.09}$	$-0.505^{+0.285}_{-0.250}$	$0.918^{+1.276}_{-1.107}$	4.8	53.0	130.5
[23,38]	$67.34^{+2.16}_{-2.12}$	$-0.485^{+0.272}_{-0.249}$	$0.809^{+1.351}_{-1.073}$	3.2	53.6	150.0
[38,53]	$67.59^{+1.73}_{-1.81}$	$-0.513^{+0.262}_{-0.227}$	$0.907^{+1.273}_{-1.118}$	2.6	47.6	132.8
[53,68]	$67.49^{+1.53}_{-1.61}$	$-0.512^{+0.250}_{-0.219}$	$0.929^{+1.231}_{-1.095}$	2.3	45.7	125.6
[68,83]	$67.27^{+1.44}_{-1.48}$	$-0.488^{+0.235}_{-0.222}$	$0.837^{+1.225}_{-1.011}$	2.2	47.0	133.6
[83,98]	$67.26^{+1.34}_{-1.37}$	$-0.461^{+0.225}_{-0.220}$	$0.651^{+1.228}_{-0.980}$	2.0	48.3	170.4
[98,113]	$67.68^{+1.17}_{-1.24}$	$-0.526^{+0.220}_{-0.195}$	$0.948^{+1.261}_{-1.169}$	1.8	39.5	128.6
[113,128]	$67.62^{+1.19}_{-1.24}$	$-0.523^{+0.217}_{-0.191}$	$0.927^{+1.236}_{-1.240}$	1.8	38.9	138.8
[128,143]	$67.39^{+1.11}_{-1.12}$	$-0.494^{+0.201}_{-0.186}$	$0.898^{+1.347}_{-1.240}$	1.6	39.2	144.6
[143,158]	$67.61^{+1.23}_{-1.24}$	$-0.521^{+0.202}_{-0.185}$	$0.887^{+1.351}_{-1.244}$	1.8	37.1	146.2
[158,173]	$67.70^{+1.27}_{-1.27}$	$-0.525^{+0.209}_{-0.191}$	$0.907^{+1.377}_{-1.277}$	1.9	38.1	146.4
[173,188]	$67.69^{+1.23}_{-1.23}$	$-0.531^{+0.206}_{-0.194}$	$0.913^{+1.353}_{-1.278}$	1.8	37.7	144.5
[188,203]	$67.84^{+1.35}_{-1.35}$	$-0.536^{+0.225}_{-0.205}$	$0.900^{+1.352}_{-1.264}$	2.0	40.1	145.3
[203,218]	$67.53^{+1.37}_{-1.32}$	$-0.501^{+0.229}_{-0.218}$	$0.989^{+1.328}_{-1.308}$	2.0	44.6	133.3
[218,233]	$67.48^{+1.36}_{-1.32}$	$-0.507^{+0.244}_{-0.232}$	$0.969^{+1.341}_{-1.304}$	2.0	47.0	136.0
[233,248]	$67.57^{+1.50}_{-1.43}$	$-0.511^{+0.261}_{-0.253}$	$0.989^{+1.325}_{-1.318}$	2.2	50.3	133.7
[248,263]	$67.39^{+1.44}_{-1.33}$	$-0.462^{+0.266}_{-0.272}$	$1.040^{+1.345}_{-1.318}$	2.1	58.0	128.7
[263,278]	$67.67^{+1.27}_{-1.21}$	$-0.522^{+0.263}_{-0.254}$	$0.941^{+1.359}_{-1.312}$	1.8	49.8	142.5
[278,293]	$67.38^{+1.34}_{-1.23}$	$-0.502^{+0.276}_{-0.253}$	$1.018^{+1.326}_{-1.312}$	1.9	52.7	129.5
[293,308]	$67.64^{+1.24}_{-1.22}$	$-0.493^{+0.282}_{-0.271}$	$0.998^{+1.342}_{-1.333}$	1.8	56.0	134.1
N						
100	$67.45^{+0.93}_{-0.98}$	$-0.500^{+0.194}_{-0.180}$	$0.879^{+1.091}_{-0.976}$	1.4	37.4	117.5
150	$67.65^{+0.76}_{-0.80}$	$-0.542^{+0.167}_{-0.152}$	$1.100^{+0.954}_{-0.898}$	1.2	29.4	84.4
200	$67.50^{+0.77}_{-0.78}$	$-0.485^{+0.154}_{-0.154}$	$0.744^{+0.911}_{-0.780}$	1.1	31.8	113.5
250	$67.66^{+0.64}_{-0.68}$	$-0.536^{+0.140}_{-0.129}$	$1.087^{+0.797}_{-0.763}$	1.0	25.1	71.5
300	$67.71^{+0.59}_{-0.61}$	$-0.541^{+0.128}_{-0.123}$	$1.083^{+0.766}_{-0.709}$	0.9	23.1	68.1
350	$67.60^{+0.52}_{-0.54}$	$-0.518^{+0.115}_{-0.111}$	$0.934^{+0.679}_{-0.630}$	0.8	21.9	70.9
400	$67.72^{+0.53}_{-0.55}$	$-0.542^{+0.116}_{-0.111}$	$1.068^{+0.694}_{-0.646}$	0.8	21.0	63.1
450	$67.66^{+0.45}_{-0.45}$	$-0.521^{+0.100}_{-0.098}$	$0.938^{+0.604}_{-0.560}$	0.7	19.1	62.1
500	$67.65^{+0.44}_{-0.45}$	$-0.534^{+0.098}_{-0.093}$	$1.045^{+0.584}_{-0.555}$	0.7	17.9	54.6
550	$67.84^{+0.42}_{-0.44}$	$-0.572^{+0.094}_{-0.089}$	$1.267^{+0.573}_{-0.554}$	0.6	16.0	44.4

Table 5: Cosmographic parameter estimates for the ET interferometer as a function of the signal-to-noise ratio and the number of detected events.

SNR interval / N	H_0 (Km/s/Mpc)	q_0	j_0	σ_{H_0}/H_0 (%)	$\sigma_{q_0}/ q_0 $ (%)	σ_{j_0}/j_0 (%)
SNR Intervals						
[8,48]	$67.91^{+7.74}_{-7.48}$	$-0.508^{+0.317}_{-0.293}$	$1.004^{+1.274}_{-1.306}$	11.2	60.1	128.6
[48,88]	$67.14^{+1.94}_{-1.96}$	$-0.467^{+0.261}_{-0.257}$	$0.765^{+1.263}_{-0.921}$	2.9	55.6	142.3
[88,128]	$67.62^{+1.00}_{-1.07}$	$-0.524^{+0.158}_{-0.148}$	$1.016^{+0.776}_{-0.699}$	1.5	29.1	72.6
[128,168]	$67.81^{+0.66}_{-0.66}$	$-0.555^{+0.104}_{-0.104}$	$1.132^{+0.573}_{-0.511}$	1.0	18.7	47.9
[168,208]	$67.69^{+0.48}_{-0.47}$	$-0.540^{+0.077}_{-0.078}$	$1.056^{+0.427}_{-0.388}$	0.7	14.4	38.6
[208,248]	$67.62^{+0.40}_{-0.40}$	$-0.525^{+0.065}_{-0.066}$	$0.970^{+0.360}_{-0.329}$	0.6	12.5	35.4
[248,288]	$67.67^{+0.35}_{-0.35}$	$-0.532^{+0.058}_{-0.059}$	$0.987^{+0.323}_{-0.298}$	0.5	10.9	31.5
[288,328]	$67.72^{+0.32}_{-0.31}$	$-0.539^{+0.053}_{-0.054}$	$1.033^{+0.300}_{-0.278}$	0.5	9.9	28.1
[328,368]	$67.67^{+0.32}_{-0.32}$	$-0.533^{+0.055}_{-0.055}$	$1.001^{+0.311}_{-0.289}$	0.5	10.3	30.0
[368,408]	$67.70^{+0.36}_{-0.35}$	$-0.539^{+0.068}_{-0.069}$	$1.040^{+0.416}_{-0.384}$	0.5	12.7	38.5
[408,448]	$67.67^{+0.41}_{-0.41}$	$-0.531^{+0.084}_{-0.085}$	$0.992^{+0.545}_{-0.501}$	0.6	16.0	53.1
[448,488]	$67.67^{+0.44}_{-0.45}$	$-0.537^{+0.099}_{-0.100}$	$1.051^{+0.670}_{-0.627}$	0.7	18.5	61.6
[488,528]	$67.59^{+0.48}_{-0.48}$	$-0.512^{+0.113}_{-0.112}$	$0.856^{+0.801}_{-0.740}$	0.7	21.9	89.4
[528,568]	$67.64^{+0.51}_{-0.51}$	$-0.521^{+0.126}_{-0.125}$	$0.927^{+0.935}_{-0.864}$	0.8	24.1	97.1
[568,608]	$67.61^{+0.52}_{-0.52}$	$-0.511^{+0.133}_{-0.134}$	$0.804^{+1.052}_{-0.946}$	0.8	26.1	124.3
[608,648]	$67.54^{+0.50}_{-0.50}$	$-0.506^{+0.136}_{-0.134}$	$0.816^{+1.105}_{-1.018}$	0.7	26.7	130.5
[648,688]	$67.64^{+0.50}_{-0.52}$	$-0.523^{+0.143}_{-0.138}$	$0.920^{+1.134}_{-1.089}$	0.8	26.9	121.5
[688,728]	$67.70^{+0.48}_{-0.50}$	$-0.534^{+0.141}_{-0.133}$	$0.995^{+1.197}_{-1.172}$	0.7	25.7	119.1
[728,768]	$67.65^{+0.48}_{-0.50}$	$-0.533^{+0.135}_{-0.133}$	$1.014^{+1.246}_{-1.201}$	0.7	25.2	120.4
[768,808]	$67.71^{+0.48}_{-0.49}$	$-0.530^{+0.137}_{-0.136}$	$0.867^{+1.320}_{-1.214}$	0.7	25.8	146.1
N						
800	$67.73^{+0.30}_{-0.30}$	$-0.544^{+0.054}_{-0.055}$	$1.068^{+0.314}_{-0.290}$	0.4	10.0	28.3
1000	$67.69^{+0.27}_{-0.27}$	$-0.537^{+0.048}_{-0.049}$	$1.020^{+0.276}_{-0.260}$	0.4	9.0	26.2
1200	$67.67^{+0.24}_{-0.24}$	$-0.536^{+0.043}_{-0.044}$	$1.025^{+0.248}_{-0.235}$	0.4	8.1	23.6
1400	$67.65^{+0.22}_{-0.22}$	$-0.530^{+0.040}_{-0.040}$	$0.987^{+0.226}_{-0.215}$	0.3	7.5	22.4
1600	$67.65^{+0.21}_{-0.21}$	$-0.534^{+0.038}_{-0.038}$	$1.019^{+0.213}_{-0.205}$	0.3	7.1	20.6
1800	$67.68^{+0.20}_{-0.20}$	$-0.538^{+0.036}_{-0.036}$	$1.038^{+0.203}_{-0.194}$	0.3	6.7	19.1
2000	$67.66^{+0.19}_{-0.19}$	$-0.535^{+0.034}_{-0.034}$	$1.024^{+0.190}_{-0.186}$	0.3	6.4	18.4
2200	$67.60^{+0.18}_{-0.18}$	$-0.524^{+0.032}_{-0.032}$	$0.952^{+0.179}_{-0.172}$	0.3	6.1	18.4
2400	$67.66^{+0.17}_{-0.17}$	$-0.534^{+0.031}_{-0.031}$	$1.005^{+0.174}_{-0.168}$	0.3	5.8	17.1
2600	$67.66^{+0.17}_{-0.17}$	$-0.534^{+0.030}_{-0.030}$	$1.008^{+0.167}_{-0.161}$	0.3	5.6	16.3

Table 6: Cosmographic parameter estimates for the DECIGO interferometer as a function of the signal-to-noise ratio and the number of detected events.